ISSN 2004-2965 Energy Proceedings, Vol. 24, 2021

International Conference on Applied Energy 2021
Nov. 29 - Dec. 5, 2021, Thailand/Virtual
Paper ID: 783

An Optical-Thermal Coupled Model for Performance Analysis of a Molten-Salt Solar Power Tower

Yu Qiu[1,2], Yuanting Zhang[1], Ya-Ling He[2,*] , Jikang Wang[1], Xiao-Yue Li[2], Qing Li[1]

1 School of Energy Science and Engineering, Central South University, Changsha, Hunan, 410083, China

2 Key Laboratory of Thermo-Fluid Science and Engineering of Ministry of Education, School of Energy and Power Engineering, Xi'an Jiaotong University, Xi'an, Shaanxi, 710049, China

(*Corresponding Author, yalinghe@mail.xjtu.edu.cn)

ABSTRACT

An optical-thermal coupled model was developed to study the performance of a typical molten-salt solar power tower, which was proven to be reliable by comparing with testing data. It is found that the mean absolute deviations between simulation and testing data are about 0.8% for the receiver efficiency under full-power condition. The model reveals that the detailed distributions of the solar flux and temperature in the receiver are extremely non-uniform, which resulted in high thermal stress at the tube crown. Moreover, failure analysis of the receiver indicates that the high strain introduced by high flux can result in fatigue failure, but it can be avoided by reasonable aiming strategy. The validated model and results from this work can offer helps for appropriate performance predictions in solar power tower.

Keywords: Optical-thermal coupled model, Molten-salt receiver, Heat loss, Efficiency, Failure analysis

NONMENCLATURE

Abbreviations	
A	area (m^2)
c_p	specific heat capacity (J·kg^{-1}·K^{-1})
D, L	receiver diameter and height, respectively
E	Young's modulus (GPa)
F	view factor
g	acceleration of gravity (m·s^{-2})
Gr	Grashof number
h	convective heat transfer coefficient (W·m^{-2}·K^{-1})
H_{ref}	reference elevation (m)
$H_{\mathbf{O}}$	Height of receiver center (m)
i, j, k, m, n	variables
k_{flux}	scale factor for the aiming strategy
L	receiver effective height (m)
N_c	flow circuit number
N_p	panel number in each circuit
N_t	tube number in each panel
N_s	segment number in each tube
N_e	number of circumferential elements
Nu	Nusselt number
$\mathbf{O}$	receiver center
Pr	Prandtl number
Q	power (MW)
Q_{abs}	optical power absorbed by coating (MW)
Q_{htf}	power transferred to salt (MW)
Q_{inc}	incident power on receiver (MW)
Q_{loss}	total heat loss (MW)
q	heat transfer rate of an element (W)
r	radius (mm, m)
Re	Reynolds number
T	temperature (K, °C)
v	velocity (m·s^{-1})
$X_rY_rZ_r$	receiver Cartesian coordinate system
β_V	volume expansion coefficient (K^{-1})
γ	linear thermal expansion coefficient (m·m^{-1}·K^{-1})
ε_3	coating emissivity
η_R	receiver efficiency
ϑ	angle variable around a tube (°)
λ	conductivity (W·m^{-1}·K^{-1})
μ	dynamic viscosity (kg·m^{-1}·s^{-1})
ν	Poisson's ratio.
ρ	density (kg·m^{-3})
$\sigma_{3,crown}$	thermal stress at tube crown (MPa)
σ_{sb}	Stefan-Boltzmann constant
crown	parameter at tube crown
e	element parameter
s	parameter of segment
t	tube
1, 2, 3	parameters of salt, tube inner and outer walls, respectively
4, 5, 6	parameters of air, sky, and ground, respectively

1. INTRODUCTION

Solar power tower (SPT) is a promising technology for large-scale solar power generation. The typical SPT uses a heliostat field to concentrate solar irradiation to a molten-salt receiver. The optical-thermal performance of the collector directly influences the plant performance. However, direct measurements of the incident solar power on the practical receiver, and of the receiver temperature and thermal stress are impracticable during the realistic operation [1]. Therefore, it is necessary to develop simulation models for predicting its optical-thermal performance, which can offer helps to the performance evaluation in the plant design and to the collector control in plant operation.

Logie et al.[2] investigated on the heat transfer of liquid salt in a single receiver tube, finding that the receiver efficiency (η_R) of 0.851-0.898 can be obtained under different conditions. Boerema et al.[3] and Conroy et al.[4] analyzed the heat transfer of sodium in a receiver panel, finding that the η_R of 0.912 can be achieved. Moreover, Singer et al.[5] analyzed the efficiency of a whole molten-salt receiver, but they assumed that the tube wall temperature remains unchanged in the circumferential direction. It was found that η_R of larger than 0.85 can be achieved under the design condition. Although some models have been developed, most of them did not consider a whole receiver or the detailed temperature/flux distributions. It is also difficult to validate these models directly due to the lack of corresponding experimental data.

To better predict the optical-thermal performance, this work focuses on developing an optical-thermal coupled model by combing ray tracing and analytical methods. Based on this model, the heat transfer characteristics in the receiver will be studied.

2. PHYSICAL MODEL

Solar Two collector that located at 34.872N, 116.834W was regarded as the physical model. A sketch of the collector is illustrated in Fig. 1. The receiver consists of 2 circuits (see Fig. 2b), and each circuit includes 12 panels that are made of 316 stainless steel (see Fig. 3). In the receiver, a binary nitrate (KNO_3-$NaNO_3$, 40-60 wt.%) is heated from 290°C to 565°C. The main parameters of Solar Two are given in Table 1.

3.OPTICAL-THERMAL COUPLED MODEL

Solar radiation transfer and absorption in the collector, heat transfer process in the receiver, and corresponding thermal stress introduced by non-uniform temperature were simulated by developing an optical-thermal coupled model. In this model, the solar radiation transfer was simulated using Monte Carlo ray tracing (MCRT) method. The heat transfer in the receiver was modeled using Conjugate Heat Transfer Analysis (CHTA) method. The maximum thermal stress and strain at the tube crown were analyzed using a simplified one-dimensional model.

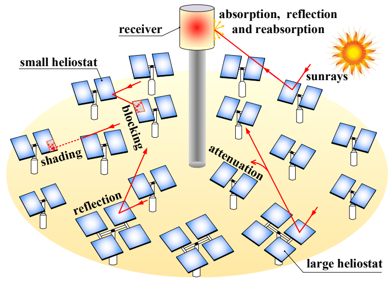

Fig. 1. Schematic of Solar Two collector.

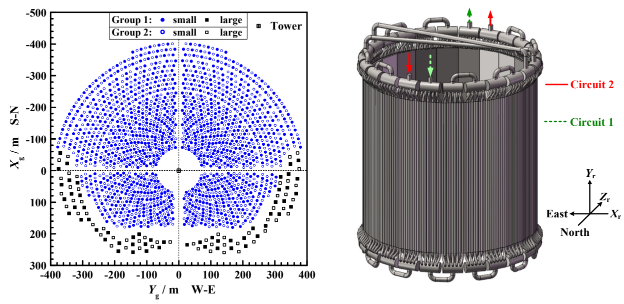

(a) Heliostat field (b) Receiver

Fig. 2. Sketches of the field and receiver of Solar Two[1].

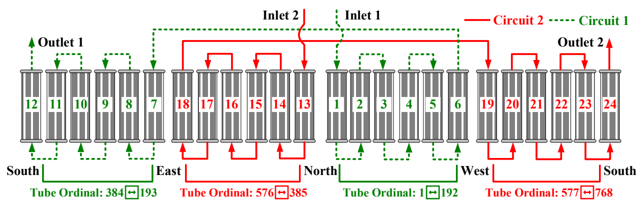

Fig. 3. Two flow circuits in the receiver.

3.1 *Optical simulation*

When the solar rays transfer in the collector, they would interact with the heliostats and receivers. These interactions are illustrated in Fig. 1. A MCRT software called SPTOPTIC [6] was employed to simulate all these interactions. Moreover, a multi-point aiming strategy[7] that can adjust the aiming points of the heliostats using a scale factor (k_{flux}) was employed. The smaller the k_{flux} is, the more dispersive the aiming points are.

3.2 *Thermal simulation*

The thermal simulation is detailed as follows.

3.2.1 Thermal balance

Heat transfer and flow in the receiver is assumed to be steady. Fig. 4 illustrates the heat transfer processes in the receiver tube. For the tube backs far from the solar radiation, the boundary can be treated as adiabatic [3].

Table 1 Parameters of Solar Two collector[1].

Parameters	Values
Small heliostat number	1818
Small heliostat area	39.13 m^2
Small heliostat center height	3.82 m
Large heliostat number	108
Large heliostat area	95 m^2
Large heliostat center height	5.79 m
Area weighted reflectivity	Case by case [1]
Heliostat cleanliness	Case by case [1]
Heliostat availability	Case by case [1]
Receiver center above ground H_O	76.2 m
Flow circuits N_c	2
Panels in each circuit N_p	12
Tubes in each panel N_t	32
Tube outer radius r_3	10.5 mm
Tube wall thickness	1.2 mm
Receiver effective height L	6.2 m
Receiver diameter D	5.1 m
RMS beam tracking error σ_{bt}	5.86 mrad
Heliostat slope error σ_{se}	1.3 mrad [8]
Solar absorptivity of coating	0.94
Diffuse reflectance of coating	0.06

The heat transfer at the tube front can be divided into two parts. One is the inward heat transfer from the outer tube wall to the heat transfer fluid (HTF), which includes the conductive heat transfer in the tube wall ($q_{e,32}$) and the convective heat transfer from the tube inner wall to the HTF ($q_{e,21}$). The other part is the outward heat transfer from the tube outer wall to the surroundings, which consists of the convective heat transfer between the tube outer wall and air ($q_{e,34}$), and the radiative heat transfer from the tube outer wall to the ground and sky ($q_{e,356}$). Considering all these heat transfer processes and the irradiation absorbed by coating ($q_{e,abs}$), an energy balance of each element is reached among $q_{e,abs}$, $q_{e,32}$, $q_{e,34}$, and $q_{e,356}$ (see Eq.(1)).

$$q_{e,abs} = q_{e,32} + q_{e,34} + q_{e,356} \tag{1}$$

where "e" represents the parameters of the elements.

3.2.2 Inward heat transfer

$q_{e,32}$ is calculated by Eq.(2). $q_{e,21}$ which equals to $q_{e,32}$ is calculated by Eq.(3), where the average convective heat transfer coefficient ($h_{s,21}$) of corresponding segment is used (see Eq.(4)) [9]. $h_{s,21}$ is predicted by Eq.(5)[10] .

$$q_{e,32} = \frac{A_{e,3}\lambda_{e,23}\left(T_{e,3} - T_{e,2}\right)}{r_3 \cdot \ln\left(r_3 / r_2\right)} \tag{2}$$

$$q_{e,21} = A_{e,2}h_{s,21}\left(T_{e,2} - T_{s,1}\right) \tag{3}$$

$$h_{s,21} = Nu_{s,21}\lambda_{s,1} / (2r_2) \tag{4}$$

$$\begin{gathered} Nu_{s,21} = 0.0154 \cdot Re_{s,1}^{0.853} \cdot Pr_{s,1}^{0.35} \cdot \left(\mu_{s,1}/\mu_{s,2}\right)^{0.14} \\ \mu_{s,1}/\mu_{s,2} = 1.01 \sim 1.31, Re_{s,1} = 10^4 \sim 10^5, Pr_{s,1} = 3.3 \sim 34 \end{gathered} \tag{5}$$

where "s,1" and "s,2" indicate that the qualitative temperatures are the average fluid temperature $T_{s,1}$ (see Eq.(6)) and the average inner wall temperature $T_{s,2}$ (see Eq.(7)) of the segment, respectively; $T_{e,2}$ is the temperature of the element at inner wall; $A_{e,2}$ is area of the element.

$$T_{s,1} = \left(T_{s,out} + T_{s,in}\right) / 2 \tag{6}$$

$$T_{s,2} = \frac{1}{N_e}\sum_{n=1}^{N_e} T_{e,2}(n) \tag{7}$$

where $T_{s,in}$ and $T_{s,out}$ are the inlet and outlet temperatures of a segment, respectively.

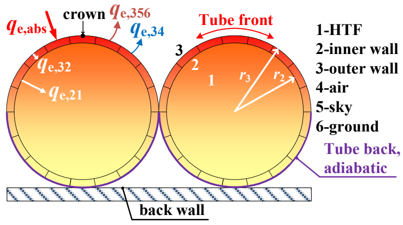

Fig. 4. Schematic of heat transfer in receiver.

3.2.3 Outward heat loss

$q_{e,34}$ is a mixed result of forced convection and natural convection and is calculated by Eq.(8). In the calculation, all tube surfaces illuminated by incident solar radiation are assumed to have the same total convective heat transfer coefficient (h_{34}) which was estimated by combining the forced and natural convective heat transfer coefficients (h_{fc}, h_{nc}) using Eq.(9)[11].

$$q_{e,34} = h_{34}A_{e,3}\left(T_{e,3} - T_4\right) \tag{8}$$

$$h_{34} = \left(h_{nc}^{3.2} + h_{fc}^{3.2}\right)^{1/3.2} \Big/ \frac{\pi}{2} \tag{9}$$

When the wind blows across a cylindrical receiver, h_{fc} can be calculated by Eqs.(10)-(13)[11]. In case that the (r_3/D) is between the (r_3/D) values of two equations, a linear interpolation between the equations will be implemented. The Reynolds number was defined in Eq.(14), where the wind speed at H_O was estimated using the speed (v_{ref}) measured at H_{ref} as shown in Eq.(14) [1].

$$h_{fc} = \frac{Nu_{fc} \cdot \lambda_{34}}{D} \tag{10}$$

$$r_3 / D = 0: Nu_{fc} = 0.3 + 0.488Re_D^{0.5}\left[1.0 + \left(\frac{Re_D}{282000}\right)^{0.625}\right]^{0.8} \tag{11}$$

$$r_3 / D = 7.5\times10^{-4}: Nu_{fc} = \begin{cases} \text{Eq.(11)}, Re_D \le 7\times10^5 \\ 2.57\times10^{-3}Re_D^{0.98}, 7\times10^5 < Re_D < 2.2\times10^7 \\ 0.0455Re_D^{0.81}, Re_D \ge 2.2\times10^7 \end{cases} \tag{12}$$

$$r_3 / D = 30\times10^{-4} : Nu_{fc} = \begin{cases} \text{Eq.}(11), Re_D \le 1.8\times10^5 \\ 0.0135 Re_D^{0.89}, 1.8\times10^5 < Re_D < 4\times10^6 \\ 0.0455 Re_D^{0.81}, Re_D \ge 4\times10^6 \end{cases} \quad (13)$$

$$Re_D = \frac{\rho_{34} D v_w}{\mu_{34}}, v_w = v_{ref}\left(\frac{H_O}{H_{ref}}\right)^{0.15} \quad (14)$$

where all air properties (c_{p34}, λ_{34}, ρ_{34}, μ_{34}) were evaluated at $\overline{T_{34}} = \left(\overline{T_3} + T_4\right)/2$; $\overline{T_3}$ is the average temperature of the tube outer walls illuminated by solar radiation.

h_{nc} on the illuminated surfaces is estimated using Eq.(15)-(16)[11].

$$h_{nc} = Nu_{nc}\lambda_4 / L \cdot \frac{\pi}{2} \quad (15)$$

$$Nu_{nc} = 0.098 Gr_L^{1/3}\left(\overline{T_3}/T_4\right)^{0.625}, Gr_L = \left(\overline{T_3} - T_4\right) g \beta_V L^3 \rho_4^2 / \mu_4^2 \quad (16)$$

where all air properties are evaluated at T_4.

The radiative view factor ($F_{e,3456}$) from the element on the tube to the environment can be divided into the view factor to sky ($F_{e,35}$) and the view factor to the ground ($F_{e,36}$). The total radiative heat loss from each element ($q_{e,356}$) is calculated by Eq.(18) [12]. In the calculation, the ground temperature (T_6) was assumed to be equal to T_4, and the sky temperature was estimated by Eq.(19)[13].

$$F_{e,356} = F_{e,35} + F_{e,36}, \quad F_{e,36} = F_{e,35} \quad (17)$$

$$\begin{aligned} q_{e,356} &= \sigma_{sb}\varepsilon_{e,3}A_{e,3}\left[F_{e,35}\left(T_{e,3}^4 - T_5^4\right) + F_{e,36}\left(T_{e,3}^4 - T_6^4\right)\right] \\ \varepsilon_{e,3} &= 0.794 + 1.55\times10^{-4}\cdot T_{e,3} - 5.93\times10^{-8}\cdot T_{e,3}^2 \end{aligned} \quad (18)$$

$$T_6 = T_4, \quad T_5 = 0.0552\cdot T_4^{1.5} \quad (19)$$

where $\varepsilon_{e,3}$ is thermal emittance of the coating [14].

After computing all above processes in an iterative way, the convective and radiative heat losses from the receiver (Q_{34}, Q_{356}) is calculated by Eq.(20) and Eq.(21), respectively. The total heat loss from the receiver (Q_{loss}) is calculated by Eq.(22). The power transferred to heat transfer fluid (Q_{htf}) is obtained using Eq.(23). The receiver efficiency is calculated using Eq.(24).

$$Q_{34} = \sum_{i=1}^{N_c}\sum_{j=1}^{N_p}\sum_{k=1}^{N_t}\sum_{m=1}^{N_s}\sum_{n=1}^{N_e} q_{e,34}(n,m,k,j,i) \quad (20)$$

$$Q_{356} = \sum_{i=1}^{N_c}\sum_{j=1}^{N_p}\sum_{k=1}^{N_t}\sum_{m=1}^{N_s}\sum_{n=1}^{N_e} q_{e,356}(n,m,k,j,i) \quad (21)$$

$$Q_{loss} = Q_{34} + Q_{356} \quad (22)$$

$$Q_{htf} = Q_{abs} - Q_{loss} \quad (23)$$

$$\eta_R = Q_{htf}/Q_{inc} \quad (24)$$

3.3 Thermal stress and strain at crown

The maximum tube temperature would occur at the tube crown (see Fig. 4), which results in the highest compressive thermal stress at the crown ($\sigma_{3,crown}$). A simplified elastic thermal-stress analysis approach introduced in Ref.[15] was employed to compute the thermal stress at the crown. Firstly, the average temperature of the tube at the crown ($T_{e,23,crown}$) was calculated by Eq.(25). Then, the mean temperature of the tube cross section (T_m) was calculated by Eq.(26). Finally, the thermal stress at the crown ($\sigma_{3,crown}$) can be approximately calculated by Eq.(27).

$$T_{e,23,crown} = (T_{e,2,crown} + T_{e,3,crown})/2 \quad (25)$$

$$T_m = T_1 + 1/\pi(T_{e,23,crown} - T_1) \quad (26)$$

$$\sigma_{3,crown} \approx \gamma_{23}E_{23}\left[\left(T_{e,23,crown} - T_m\right) + \frac{T_{e,3,crown} - T_{e,2,crown}}{2\left(1-\upsilon_{23}\right)}\right] \quad (27)$$

When T=300K-1000K, E, γ, λ, and υ of the tube can be predicted by Eq.(28)[16].

$$\begin{aligned} &E = 205.91 - 2.6913\times10^{-2}T - 4.1876\times10^{-5}T^2 \ \text{GPa} \\ &\gamma = \left(11.813 + 1.3106\times10^{-2}T - 6.1375\times10^{-6}T^2\right)\times10^{-6} \ \text{m}\cdot\text{m}^{-1}\cdot\text{K}^{-1} \\ &\lambda = 9.0109 + 1.5298\times10^{-2}T \quad \text{W}\cdot\text{m}^{-1}\cdot\text{K}^{-1} \\ &\nu = 0.3 \end{aligned} \quad (28)$$

To ensure that the receiver can work safely during its 30-year lifetime, it is necessary to make sure that the receiver can withstand the fatigue caused by 36,000 nominal thermal cycles[17]. Thus, a failure analysis was conducted. Firstly, the allowable strain(ε_a) of 316 steel for 36,000 thermal cycles was obtained [18]. Then, the $\varepsilon_{3,crown}$ of the tube that has the maximum stress in each panel is evaluated using Eq.(29) at its nominal condition. Finally, if the $\varepsilon_{3,crown}$ on all tubes are lower than the ε_a, the receiver can work safely for 30 years.

$$\varepsilon_{3,crown} \approx \gamma_{23}\left[\left(T_{e,23,crown} - T_m\right) + \frac{T_{e,3,crown} - T_{e,2,crown}}{2\left(1-\upsilon_{23}\right)}\right] \quad (29)$$

3.4 Grid-independence test

To eliminate the influence of the mesh number, a grid-independence test is conducted under the full-power condition of Day 9 in Ref.[1]. η_R, Q_{loss}, and the circumferential $T_{e,3}$ at the middle of the northernmost tube in Circuit 1 are examined. It is observed in Fig. 5 that the η_R, Q_{loss} and $T_{e,3}$ vary little when the mesh is larger than 26 (N_e) × 61 (N_s). The results indicate that this mesh system is large enough.

4.RESULTS AND DISCUSSION

4.1 Simulation results vs. testing data

It is well known that accurate prediction of the receiver performance is important for the performance improvement and safety. So, the receiver performance under both full-power (i.e., Period A in Ref.[1]) condition and half-power (i.e., Period D in Ref.[1]) conditions were analysed. Under the full-power condition, all heliostats in Fig. 2a were used. Under the half-power condition, only the group 2 heliostats were used.

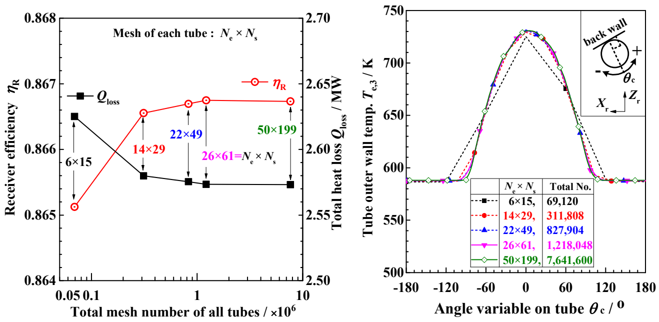

(a) η_R and Q_{loss} (b) $T_{e,3}$

Fig. 5. Effects of mesh number on simulation results.

Fig. 6 compares the simulated total heat losses (Q_{loss}) and the testing data [1]. It is found that the mean relative error between current results and the testing data is just 8.3% under the full-power condition (see Fig. 6a). Under the half-power condition, the corresponding value is 9.1% (see Fig. 6b). Moreover, it is found that the mean relative deviation between heat losses at half-power and full-power conditions is just 5.3%, indicating that heat loss is barely influenced by the incident solar power.

Fig. 6 also compares the simulated receiver efficiency (η_R) and the testing data of Pacheco et al.[1]. It is seen that the mean absolute deviation between current results and the testing data is just 0.008 under the full-power condition (see Fig. 6a), and corresponding value for the half-power condition is just 0.012 (see Fig. 6b).

The above results indicate that current model can predict the heat loss and receiver efficiency well at both full-power and half-power conditions.

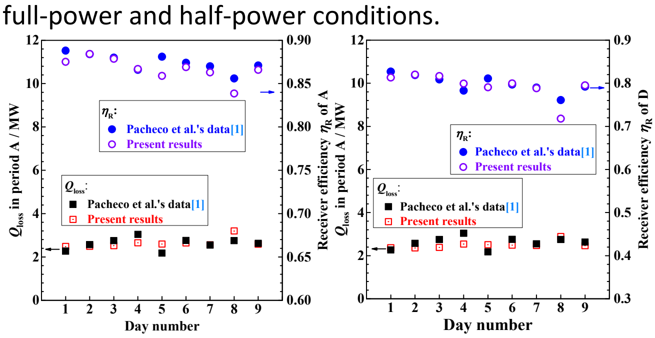

(a) Full power in Period A (b) Half power in Period D

Fig. 6. Testing obtained and simulated data in 9 days.

4.2 Distributions of the flux, temperature and stress

High temperature and thermal stress introduced by non-uniform solar flux can result in coating degradation and receiver failure, so they necessary to be detailedly predicted for preventing corresponding issues. Based on the validated model, these detailed features were analyzed at the typical condition (11.232 a.m.) in Day 9 under the full-power condition in period A [1].

Fig. 7a illustrates the flux distribution on the receiver. It is seen that the flux at the northern side is much higher than that at the southern side, because the total heliostat area at northern side is much larger, and northern heliostats also have higher optical efficiency. It can be observed that a high-flux zone occurs at the middle part of the northern side even the multi-point aiming strategy was employed.

Fig. 7b shows the temperature distribution on the tube outer walls. It can be seen that the northern side is colder than the southern side. This is because the cold salt flows into the receiver through the northernmost panels, and it is heated gradually from the north to the south. As a result, even the northern side accepts more solar radiation power, it still has lower temperature.

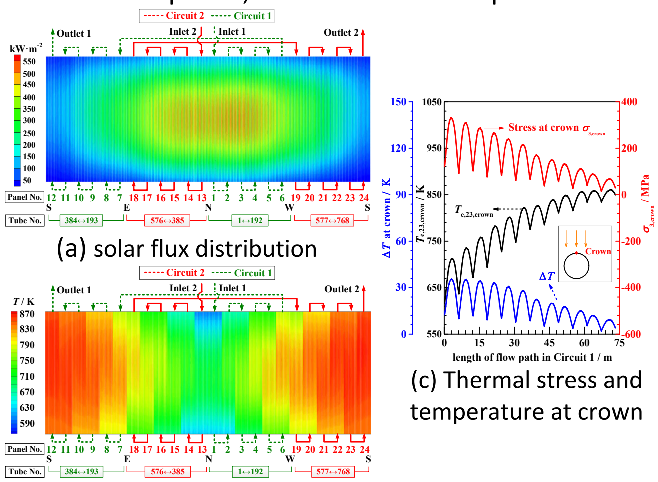

(a) solar flux distribution

(b) Temperature distribution

(c) Thermal stress and temperature at crown

Fig. 7. Distributions of the flux, temperature and stress.

It is found that a large temperature difference between the inner and outer walls (ΔT) occurs at the crown (see Fig. 7c), where the tube that has the maximum stress at the crown in each panel is selected as the representative tube. It is seen that the peak ΔT in every panel decreases with increasing flow path, and the maximum ΔT of 36K occurs at the middle of the first panel in Circuit 1. The detailed thermal stress at the tube crown ($\sigma_{3,crown}$) is also illustrated in Fig. 7c. It is observed that the peak thermal stress at the crown is around 333 MPa in the first panel. Moreover, it is seen that the peak $\sigma_{3,crown}$ in each panel decreases along the flow path.

4.3 Fatigue failure analysis

In this section, firstly, the thermal strain under the typical condition at 11.232 a.m. of Day 9 was evaluated, and the incident power was scaled up to the design incident power of 48 MW, where v_w =3 m·s^{-1} and T_4 =20°C. Under this condition, the peak flux on the absorber is 832 kW·m^{-2} when k_{flux}=1.5.

Fig. 8(a) shows the thermal strain of the tube that has the maximum strain at the crown in each panel in Circuit

1. It can be seen that the strain at most regions of the tubes are lower than the allowable strain [18], (i.e., in the safety zone). However, the high strain around the middle parts of the first five tubes are in the failure zone, indicating the receiver cannot work safely for 30 years.

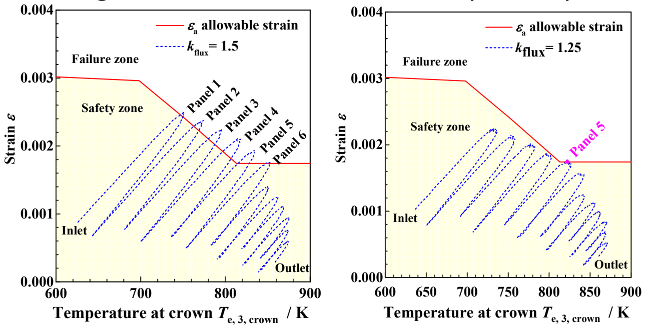

(a) k_{flux}=1.50 (b) k_{flux}=1.25

Fig. 8. Crown thermal strain under nominal incident power under different aiming scale factor.

To make the receiver work safely, the aiming strategy of the heliostats was adjusted by modifying the k_{flux}. It is found that the peak strain of panel 5 just touch the allowable strain curve in Fig. 8(b) when k_{flux}=1.25. And all other regions of the tubes are lower than the allowable strain curve. It means that the receiver would be able to work safely for 30 years if $k_{flux} \leq 1.25$.

5.CONCLUSIONS

The following conclusions are derived.

(1) The model was proven to be reliable by comparing with testing data under realistic conditions. It is found that the total heat loss of the receiver is barely influenced by the incident solar power.

(2) Detailed solar flux and temperature distributions in the receiver are revealed and are found to be extremely non-uniform, which results in corresponding high thermal stress at the tube crown. It is also found that the flux, temperature and stress at tube crown increase in a wavy pattern along the flow path.

(3) Fatigue failure analysis of the receiver indicates that the high flux can result in fatigue failure, but it can be avoided by reasonable aiming strategy.

ACKNOWLEDGEMENT

This work was supported by the National Natural Science Foundation of China (No. 52006247, 51976156, 52176093) and Hunan Provincial Natural Science Foundation (2021JJ40753).

The authors would also like to thank the Foundation for Innovative Research Groups of the National Natural Science Foundation of China (No.51721004).

REFERENCE

[1] Pacheco JE, Bradshaw RW, Dawson DB, De la Rosa W, Gilbert R, Goods SH, et al. Final test and evaluation results from the Solar Two project. Albuquerque, NM: Sandia National Laboratories; 2002, No. SAND2002-0120.
[2] Logie WR, Pye JD, Coventry J. Thermoelastic stress in concentrating solar receiver tubes: A retrospect on stress analysis methodology, and comparison of salt and sodium. Sol Energ. 2018;160: 368-79.
[3] Boerema N, Morrison G, Taylor R, Rosengarten G. High temperature solar thermal central-receiver billboard design. Sol Energ. 2013;97: 356-68.
[4] Conroy T, Collins MN, Fisher J, Grimes R. Levelized cost of electricity evaluation of liquid sodium receiver designs through a thermal performance, mechanical reliability, and pressure drop analysis. Sol Energ. 2018;166: 472-85.
[5] Singer C, Buck R, Pitz-Paal R, Müller-Steinhagen H. Assessment of solar power tower driven ultrasupercritical steam cycles applying tubular central receivers with varied heat transfer media. J Sol Energ. 2010;132(4): 041010.
[6] Qiu Y, He YL, Li PW, Du BC. A comprehensive model for analysis of real-time optical performance of a solar power tower with a multi-tube cavity receiver. Appl Energ. 2017;185: 589-603.
[7] Sanchez-Gonzalez A, Santana D. Solar flux distribution on central receivers: A projection method from analytic function. Renew Energ. 2015;74: 576-87.
[8] Osuna R. Solar thermal industry, success stories and perspectives. Renewable energy for Europe, research in action, European Commission, Brussels, 21-22, November, 2005.
[9] Yang X, Yang X, Ding J, Shao Y, Fan H. Numerical simulation study on the heat transfer characteristics of the tube receiver of the solar thermal power tower. Appl Energ. 2012;90(1): 142-7.
[10] Qiu Y, Li MJ, Li MJ, Zhang HH, Ning B. Numerical and experimental study on heat transfer and flow features of representative molten salts for energy applications in turbulent tube flow. Int J Heat Mass Tran. 2019;135: 732-45.
[11] Siebers DL, Kraabel JS. Estimating convective energy losses from solar central receivers. Livermore, U.S.A.: Sandia National Laboratories; 1984, SAND84-8717.
[12] Leon MA, Kumar S. Mathematical modeling and thermal performance analysis of unglazed transpired solar collectors. Sol Energ. 2007;81(1): 62-75.
[13] Nowak H. The sky temperature in net radiant-heat loss calculations from low-sloped roofs. Infrared Phys. 1989;29(2-4): 231-2.
[14] Ho CK, Mahoney AR, Ambrosini A, Bencomo M, Hall A, Lambert TN. Characterization of Pyromark 2500 paint for high-temperature solar receivers. J Sol Energ. 2013;136(1): 014502.
[15] Company BW. Molten salt solar receiver subsystem research experiment. Phase 1-final report. Volume 1-Technical. Albuquerque: Sandia National Laboratories; 1984, SAND82-8178.
[16] Austenitic stainless steel (316). Access time: Aug. 10, 2017, www-ferp.ucsd.edu/LIB/PROPS/PANOS/ss.html.
[17] Liao Z, Li X, Xu C, Chang C, Wang Z. Allowable flux density on a solar central receiver. Renew Energ. 2014;62: 747-53.
[18] ASME Boiler and Pressure Vessel Code-Section III. New York, NY: The American Society of Mechanical Engineers; 2013.